Design and Electromagnetic Analysis of a HTS Linear Synchronous Motor

Jianxun Jin, Luhai Zheng
Center of Applied Superconductivity and Electrical Engineering
University of Electronic Science and Technology of China
Chengdu, China
jxjin@uestc.edu.cn, zluhai@uestc.edu.cn

Youguang Guo, Jianguo Zhu
School of Electrical, Mechanical and Mechatronic Systems
University of Technology Sydney, Australia
Sydney, Australia
youguang@eng.uts.edu.au

Abstract—**High temperature superconducting (HTS) linear synchronous motor (LSM) integrated with HTS magnetic levitation system, can realize self-levitation and self-guidance without any sliding friction, which will have important applications in many fields such as electromagnetic aircraft launch system, maglev transportation. This paper presents the design and electromagnetic analysis of a HTS LSM, which is levitated by a magnetic levitation system consisting of HTS bulks-permanent magnet (PM) guideways. Numerical analysis and magnetic field finite element analysis (FEA) methods are applied to analyze the thrust, levitation and guidance force characteristics, and the electromagnetic performance of HTS LSM under no-load and load situations are studied with the analysis results are given. Finally, the primary motor running testing results are provided.**

Keywords-high temprature superconductor; HTS linear synchronous motor; electromagnetic characteristic;HTS magnetic levitation; HTS bulk

I. INTRODUCTION

A high temperature superconducting (HTS) bulk can trap higher magnetic field than a permanent magnet, and a few compact and higher-performance electric motors and linear actuators are being realized by using HTS bulks [1,2]. Now, the HTS linear synchronous motor (LSM) technology using bulk superconductor magnet (BSCM) has been developed [2-5]. Compared to the conventional linear motor, a HTS LSM has advantages, such as smaller volume, less weight, bigger propulsion, and higher power factor.

Since stable levitation force can be generated between NdFeB permanents magnets (PMs) and HTS bulks bathed in liquid nitrogen [6,7], HTS magnetic levitation system containing PMs and HTS bulks can be used in a HTS LSM to replace the conventional slide rail [8]. The main advantage of HTS magnetic levitation system is the strong levitating force with passive and self-stabilizing feature, leading to the removal of the sophisticated control system for regulating the air-gap between PM-guideway and levitated moving secondary, which is necessary for other types of levitation transportation systems. So that the HTS LSM integrated with the HTS magnetic levitation system can be applied in transportation field such as maglev, electromagnetic airplane launch system, and many other industrial automation control fields etc.

In this paper, the design of a HTS LSM levitated using a HTS levitation system is presented. Numerical analyses for thrust, levitation and guidance force characteristics are conducted with results obtained. The electromagnetic characteristics of HTS LSM under no-load and load situations are studied with the analysis results are given by finite element analysis (FEA) method. Finally, the primary LSM running testing results are presented.

II. HTS LSM MODEL

The structure model of the designed HTS LSM is shown in Fig. 1. The primary stator and the secondary rotor of the HTS LSM are composed of three-phase copper windings and YBCO BSCMs, respectively, and the magnets are put in the cryogenic vessels with alternating poles of N and S in longitudinal direction. Table I lists the major dimensions and parameters of the HTS LSM.

The HTS magnetic levitation systems are used on both sides of the HTS LSM, and the structure of the PM-guideway is shown in Fig. 2, which is consisted of PMs and assembled magnetic iron (Fe). The magnetization directions of left-side and right-side PMs are along the vertical direction, and the middle PMs are installed with opposite magnetization direction. The ferromagnet put in the middle of PMs has the function of concentrating magnetic field, and generates strong magnetic field on the upper surface of PM-guideways and weak magnetic field on the lower surface.

The HTS magnetic levitation system can realize self-levitation and self-guidance without any assistant control equipment. So that the HTS LSM can run freely without any sliding friction force with stable air-gap length.
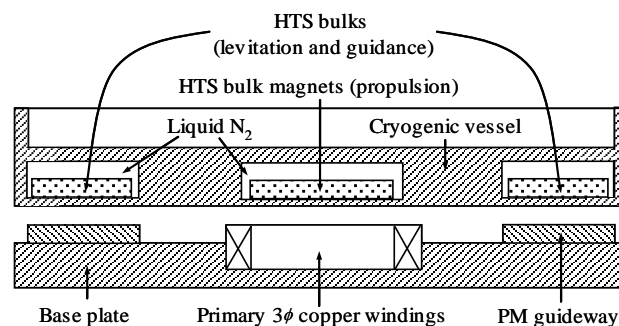

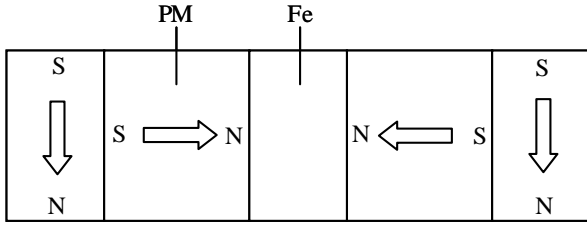Figure 1. Model of HTS LSM levitated by HTS magnetic-levitation system.

Figure 2. Structure of PM-guideway.

TABLE I. MAJOR DIMENSIONS AND PARAMETERS OF HTS LSM.

Primary	
Copper windings	
Number of turns	200
Diameter of copper wire (mm)	1.18
Resistivity ($\Omega \cdot$m)	1.75E-008
Iron core	
Tooth length (movement direction) (mm)	10
Tooth width l_t (mm)	150
Tooth depth (mm)	100
Slot width (mm)	20
Tooth pitch (mm)	30
Pole pitch τ (mm)	45
Main air gap g (mm)	6
Secondary	
BSCM	
BSCM length (movement direction) l_s (mm)	45
BSCM width w_s (mm)	45
BSCM height h_s (mm)	12
BSCM trapping field B (T)	0.35
Number of BSCMs	6
Back iron thickness (mm)	10
Running parameters	
Frequency (Hz)	10
Phase voltage (V)	165
Phase current (A)	3.3
Phase resistance (Ω)	27
Thrust force (N)	363

III. NUMERICAL ANALYSIS OF HTS LSM

A. Thrust Force Analysis

The transverse section and longitudinal section of the HTS LSM are shown in Fig. 3. The length of HTS bulks l_s is equal to the pole pitch τ with no gap between them. Neglecting the magnetic resistance of primary iron-core and back-iron, the magnetic flux one coil applied by one pole-pairs of BSCMs as
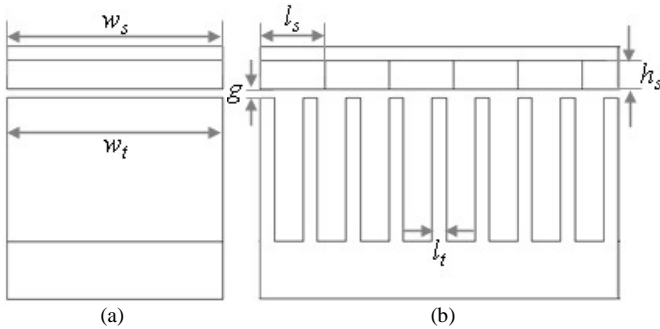

(a)   (b)

Figure 3. Model of HTS LSM (a) transverse section, (b) longitudinal section..

$$\psi_{\text{BSCM}} = \frac{\mathscr{F}}{R_{\text{tot}}} = \frac{H_c \cdot h_s}{h_s / \mu_r \mu_0 l_s w_s + g / \left[\mu_0 \cdot (l_s + l_t)/2 \cdot (w_s + w_t)/2 \right]}$$
$$= \frac{\mu_0 H_c h_m l_m w_m (l_s + l_m)(w_m + w_s)}{4 g l_m w_m + h_m l_m w_m + h_m l_m w_s + h_m l_s w_m + h_m l_s w_s} \quad (1)$$

where $\mathscr{F}$ is the magnetic potential of magnetic circuit, R_{tot} the total magnetic resistance, R_s the magnetic resistance of BSCM, R_g the magnetic resistance of air-gap, μ_r the relative permeability of BSCM ($\mu_r = 1$), H_c the magnetic field intensity of BSCM, μ_0 ($4\pi \times 10^{-7}$ H/m) the permeability of vacuum; l_s, w_s, and h_s the length, width and height of BSCM respectively; l_t, w_t the length and width of stator-tooth respectively. When the secondary rotor moves, an electromotive force (EMF) is induced in the stator windings. By differentiating the BSCM flux of phase winding against time, the back EMF is determined with an rms value as

$$E_{\text{rms}} = \sqrt{2} \pi f N_c k_N \psi_{\text{BSCM}} \quad (2)$$

The electromagnetic power P_{em} is

$$P_{\text{em}} = 3 \times E_{\text{rms}} \times I_1 \times \cos\varphi \quad (3)$$

So the fundamental wave electromagnetic thrust force F_{em} is

$$F_{\text{em}} = \frac{p \times P_{\text{em}}}{v} = \frac{p \times 3 \times E_{\text{rms}} \times I_1}{2\tau f} = \frac{3p}{\sqrt{2}\tau} N_c k_N I_1 \psi_{\text{BSCM}} \quad (4)$$

where f is the frequency, N_c the turns of phase winding, k_N the winding factor ($k_N = 1$ when the diametrical-pitch concentrated windings are applied), I_1 the phase current, $\cos\varphi$ the power factor, v the linear velocity, τ the pole pitch, p the pole-pairs.

Fig. 4 shows the thrust force F_x versus the thickness of BSCMs for various widths of bulk magnets. It is observed that the F_x increases with the increases of the thickness of BSCM, and tends to saturation gradually. It also shows that the more the BSCM width increases, the bigger the F_x is.
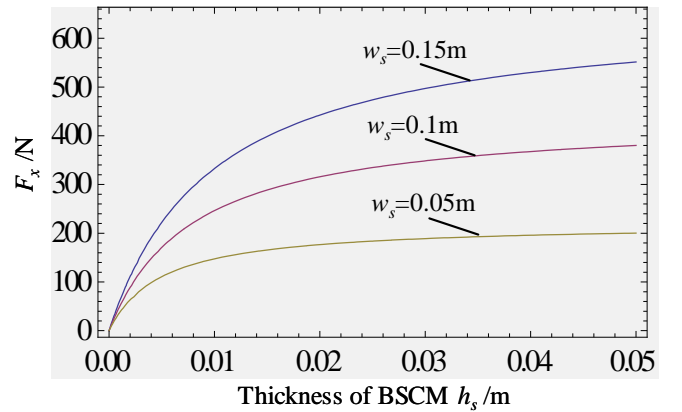

Figure 4. F_x versus h_s for different widths of BSCMs.

B. Levitation Force and Guidance Force Analysis

The levitation force and guidance force are the product of an external magnetic field and a shielding current flowing in a HTS bulk, and is calculated by the following equations

$$F_{Lev} = \int_0^{TH} \int_{L/2}^{L/2-\delta} \int_{W/2}^{W/2-\delta} J_c \times B_x \, \mathrm{d}x\mathrm{d}y\mathrm{d}z \tag{5}$$

$$F_{Gui} = \int_0^{TH} \int_{L/2}^{L/2-\delta} \int_{W/2}^{W/2-\delta} J_c \times B_z \, \mathrm{d}x\mathrm{d}y\mathrm{d}z \tag{6}$$

where F_{Lev} is the levitation force, F_{Gui} the guidance force, J_c the critical current density, B_x the field along the transverse direction, B_z the field along the vertical direction, δ the depth of field penetration. Here, it is assumed that induced shielding currents flowing in the bulk body were equal to the critical currents. The δ used as integral range is given by the following relation [9]

$$\delta = \frac{B_z - B_{zfc}}{\lambda \mu_0 J_c} \tag{7}$$

where B_{zfc} is the trapped magnetic field, λ the Nagaoka coefficient determined by the configuration of a sample. The Fig. 5 shows the interaction between a HTS bulk and the PM-guideway, and the Fig. 6 and Fig. 7 are the distributions of B_x and B_z for different heights h from upper surface of primary stator, respectively.

The relation shape between the levitation force and the distance between a HTS bulk and the PM-guideway can be described with an exponential function as follows [10]

$$\begin{cases} F = F_{Lev\_1} \exp\left(-z/\alpha_1\right) - F_{Att\_1} \exp\left(-z/\beta_1\right) & move-towards \\ F = F_{Lev\_2} \exp\left(-z/\alpha_2\right) - F_{Att\_2} \exp\left(-z/\beta_2\right) & move-away \end{cases} \tag{8}$$

where F_{Lev_1} and F_{ATT_1} are the levitation force and attractive force when HTS bulk is moved towards the PM-guideway, respectively; F_{Lev_2} and F_{ATT_2} are the levitation force and attractive force when HTS bulk is moved away the PM-guideway, respectively; α_1, α_2, β_1 and β_2 are constants, which are closely related to the superconductor and the distribution of magnetic field; z the distance between the HTS bulk and PM-guideway. Fig. 8 shows the levitation force of a HTS bulk above the PM-guideway.
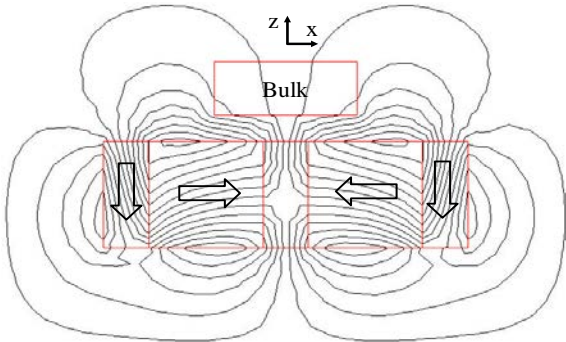
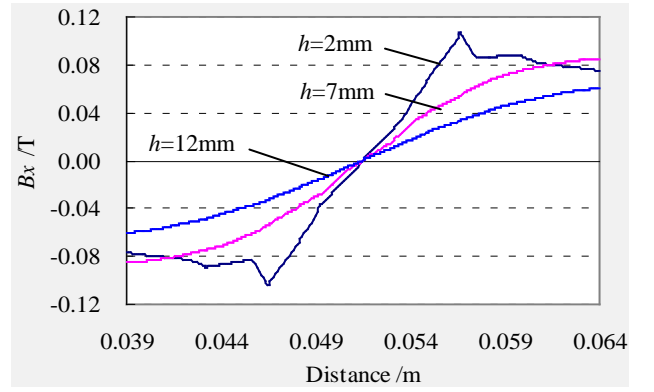Figure 5.   Model of interaction between a HTS bulk and the PM-guideway.

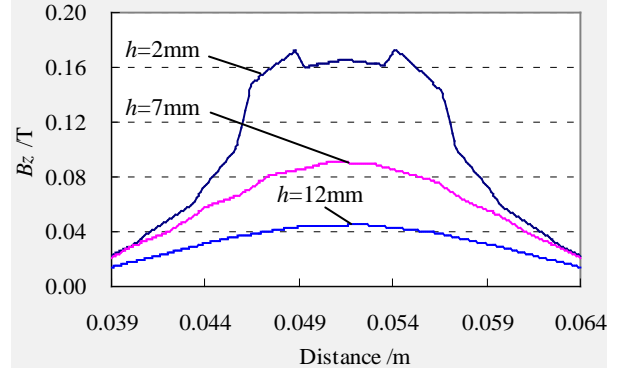Figure 6.   Distributions of B_x for different heights.

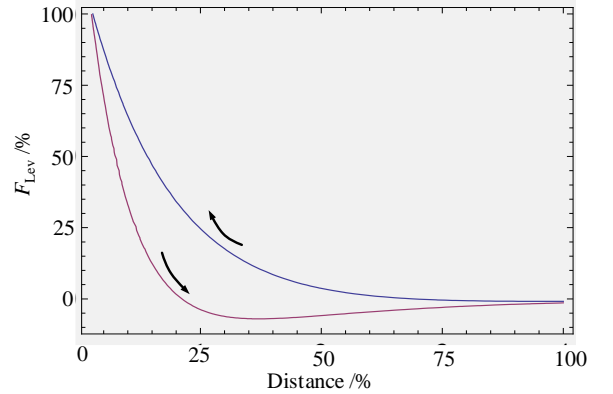Figure 7.   Distributions of B_z for different heights.

Figure 8.   The levitation force between a HTS bulk and the PM-guideway.

IV.   ELECTROMAGNETIC CHARACTERISTIC ANALYSIS OF HTS LSM

According to the above assumptions and motor geometric parameters, 2-D finite element model for the whole HTS LSM is built by the way of direct modeling method, which is sufficient for the theoretical analysis with relatively low computational complexity, and the end effect can also be considered.

The finite element model is shown in Fig. 9. The materials in model are numbered as: ① air; ② BSCM North (with the magnetization direction along the negative y-axis direction); ③ BSCM South (with the magnetization direction along the y-

axis direction): ④ BSCM back iron; ⑤ stator iron core; and ⑥ copper stranded coils. The magnetic vector potentials obey the periodical boundary conditions on the *y*-direction boundary lines of the primary stator and secondary rotor and the open middle air-gap line, and the time-stepping FEA method is applied in resolving. To simplify the analysis, the BSCM is modeled as a PM. The analysis results of no-load and load conditions of the HTS LSM are detailed as follows.
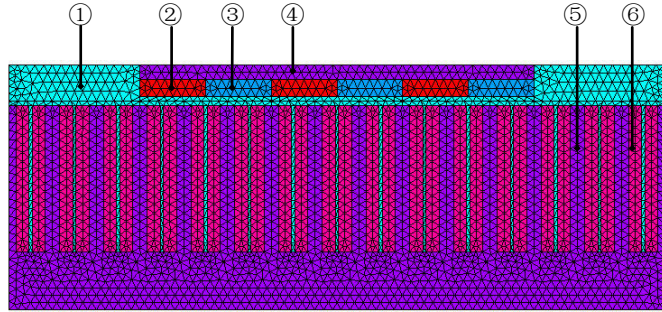
1. Air, 2. BSCM North, 3. BSCM South, 4. Back iron, 5. Iron core, 6. Coils.

Figure 9.　Finite element model of the HTS LSM.

A.　No-Load Characteristics

The distribution of magnetic flux density B_x, B_y (along the longitudinal direction), and B_{sum} (the vector sum) in middle air-gap at no-load is shown in Fig. 10.

The BSCM flux, defined as the flux of a phase winding produced by the mover BSCMs, can be determined from the magnetic field distribution at no-load. The flux waveform can be calculated by moving the rotor for one pole-pair pitch in several steps. To increase the computational accuracy and efficiency, the stator and rotor are separately meshed and keep unchanged when the rotor moves. After the meshed rotor moves to a new position, the meshes are stitched with those of the stator along the middle air-gap. For the time-stepping analysis, the meshing of middle air-gap line is controlled such that the nodes of the stator and rotor sides coincide at each step [8].

Fig. 11 shows the magnetic flux lines distribution when the rotor has moved one pitch τ from the position $x=0$, and Fig. 12 is the BSCM flux linkage characteristics one coil for various lengths of air-gap. It is showed that the flux waveform is an almost perfect sinusoid, and the flux decreases with the increase of the air-gap length.
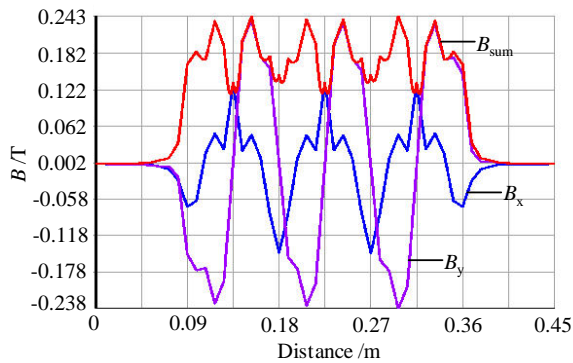

Figure 10. Distributions *of* B_x, B_y and B_{sum} along middle air-gap at no-load.

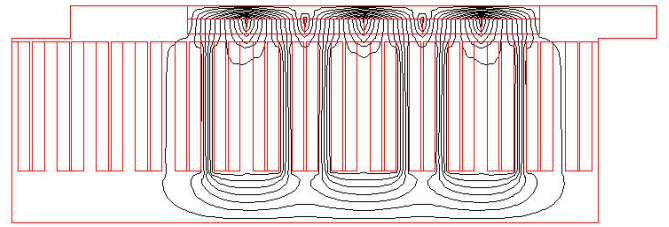
Figure 11. Distribution of magnetic flux lines when △x=τ.
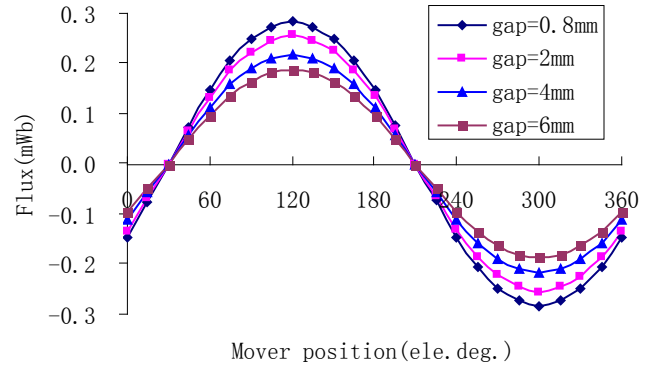

Figure 12. BSCM flux linkage characteristics one coil for various air-gap length.

B.　Load Manetic Field Distribution

The time-stepping simulation parameters as follows: the frequency *f*=10 Hz, the simulation time is one period of *T*=0.1 s, the three-phase voltage: U_a=165×sin(ωt), U_b=165×sin(ωt-2π/3), U_c=165×sin(ωt-4π/3). The solving is divided into 13 steps. In addition to the initial load step, the time period of every load step is 0.00833 s, and each step has 10 substeps with the time step size of 0.000833 s. Because it is not allowed to set time to zero in an ANSYS analysis, a very small time value of 0.1E-006 s is specified for the initial load step.

The distribution of magnetic flux lines in LSM at load is shown in Fig. 13, and Fig. 14 shows the magnetic field distribution in middle air-gap along transverse-direction and longitudinal-direction and the vector sum. As is indicated in the graph, the amplitude of magnetic flux density in air-gap is bigger than that at no-load.

Fig. 15 shows the B_{sum} in air-gap changes with the time for different air-gap heights from upper-surface of primary stator. It is observed that the field waveforms are sinusoid, and the amplitude decreases with the increases of the height. It indicates that the shorter the air-gap length is, the bigger the electromagnetic force of the rotor will be suffered.
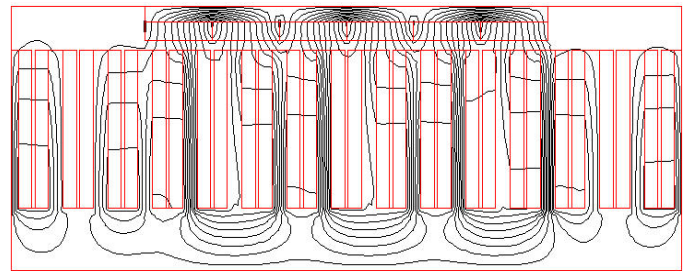

Figure 13. Distribution of magnetic flux lines at load condition.
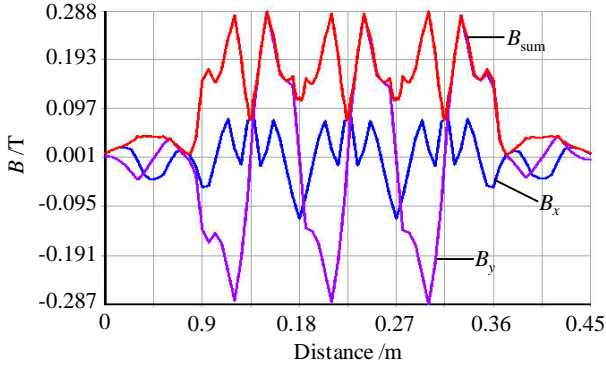
Figure 14. Distributions of B_x, B_y and B_{sum} along middle air-gap at load.
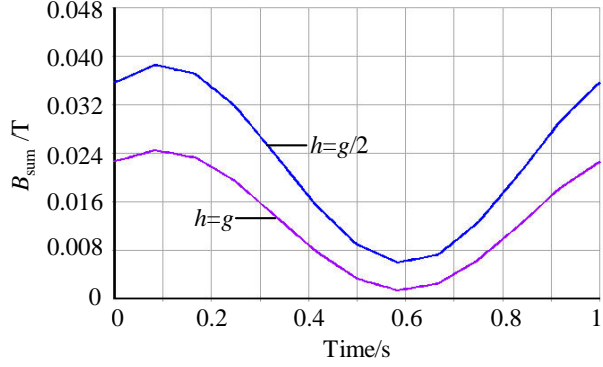

Figure 15. B_x vs. time for different air-gap heights.

C. Thrust Force Characteristics

The thrust force is directly related to the trapped magnetic field, pole-pairs and length of HTS bulks, phase current of primary windings, thickness of back-iron, and length of air-gap and so on. The relationships are calculated and the simulation results are given as follows.

The thrust force F_x versus phase current I for different trapped magnetic field B_{trr} of BSCMs is shown in Fig. 16. As can be seen from the chart, the F_x increases approximately linear with the increase of the I and the B_{trr} of BSCMs, and the F_x can reach 1000 N with $I=12$ A ($NI=240$ At) and $B_{trr}=0.35$ T, or $I=5$ A ($NI=1000$ At) and $B_{trr}=0.6$ T, or $I=3$ A ($NI=600$ At) and $B_{trr}=1$ T, or $I=2.5$ A ($NI=500$ At) and $B_{trr}=2$ T when the other parameters based on Table 1.

Fig. 17 shows the F_x versus the amount of BSCMs, which indicates that the F_x increases proportionally to the amount of HTS bulk magnets. The length of BSCM also has important influence on F_x as can be seen from Fig. 18. As is indicated in the graph, LSM will have relative bigger F_x when the ratio of the length of BSCM to the pole pitch τ is between about 4:5 and about 1:1, which will be the important reference for the design of a HTS LSM.

Fig. 19 and Fig. 20 show that the F_x and normal force F_y versus the length of air-gap for different thickness of back-iron H_{back}, respectively. It is observed that F_x and F_y decrease with the increase of the length of air-gap, and increase with the increase of the thickness of back-iron when H_{back} smaller than 10 mm. Fig. 21 shows the F_x versus the thickness of BSCM for various lengths of air-gap. The results indicate that the

appropriate thickness of BSCMs and back-iron and the length of air-gap should be selected to get an optimal F_x performance of HTS LSM.
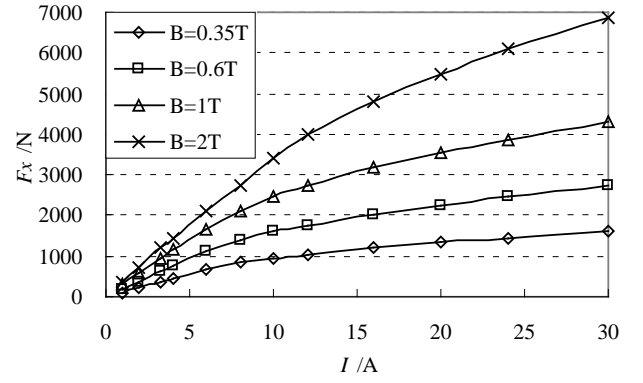

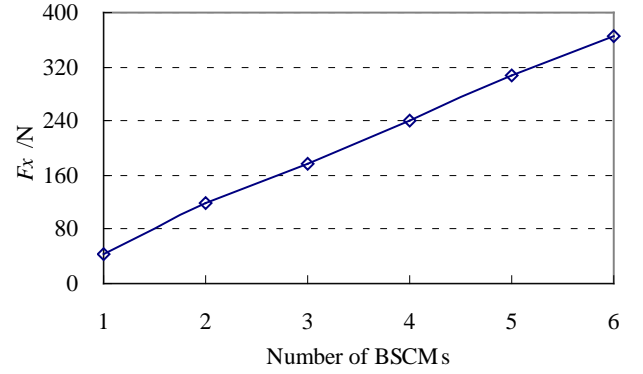Figure 16. F_x vs. the current for different trapped magnetic field of BSCMs.

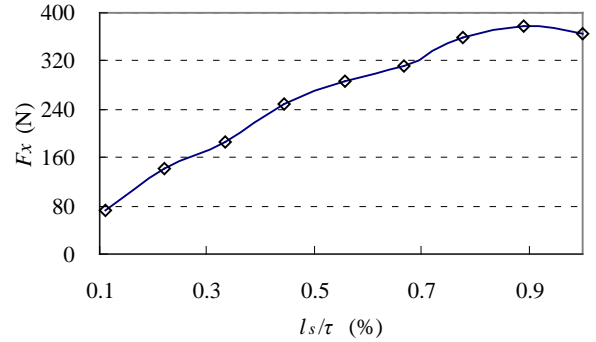Figure 17. F_x vs. the amount of BSCMs.
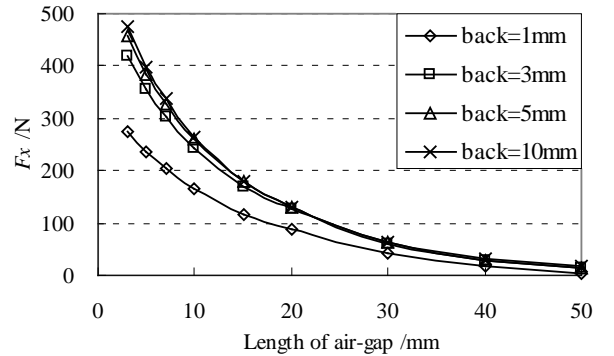

Figure 18. F_x vs. the length of BSCMs.

Figure 19. F_x vs. the length of air-gap for different thicknesses of back-iron.
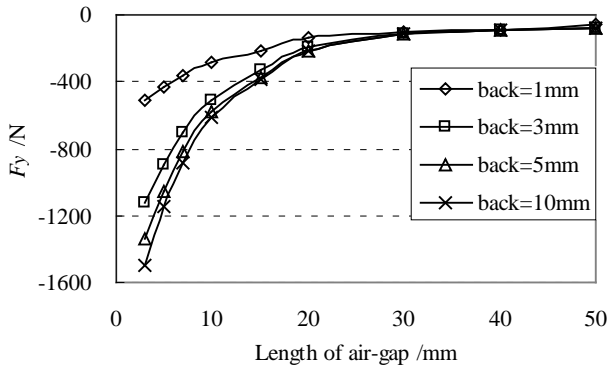
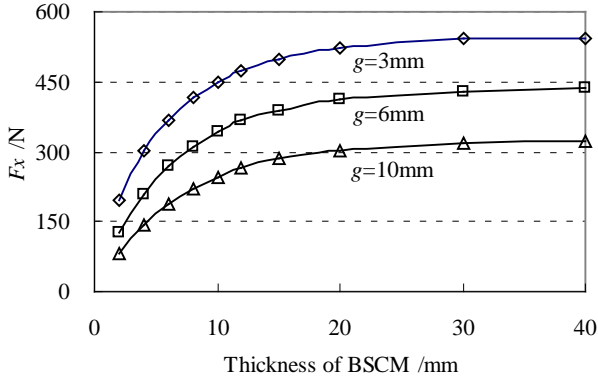Figure 20. F_y vs. the length of air-gap for different thicknesses of back-iron.

Figure 21. F_x vs. the thickness of BSCM for various lengths of air-gap.

V. TESTING RESULTS

The HTS LSM experimental device is shown in Fig. 22, which is composed of primary stator and secondary mover, and the secondary BSCMs are built in a cryogenic vessel fixed on the secondary mover, which can slide freely along the guide rails on both sides of the stator. The experimental slide rail will be replaced by the HTS levitation system.

The converter based on the Voltage Space Vector PWM (SVPWM) strategy is applied to control the running of HTS LSM. Fig. 23 shows the F_x versus the frequency for different air-gap lengths. It indicates that the F_x decrease slightly with the increase of the frequency, and the length of air-gap has great influence on F_x. Therefore the appropriate air-gap length should be selected by considering the practical requirements.

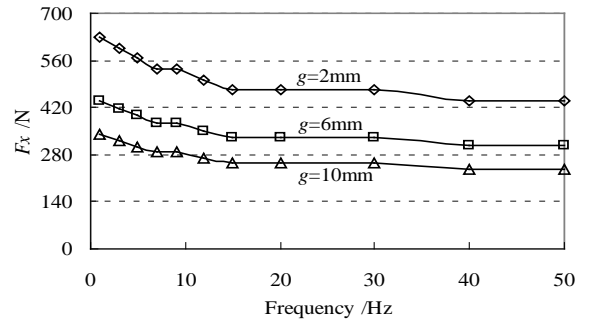Figure 22. Experimental setup of the HTS LSM.

Figure 23. F_x versus frequency for different air-gap length.

VI. CONCLUSION

The structure design of new-type HTS LSM levitated by HTS levitation system has been presented. The numerical models of thrust, levitation and guidance force were built. The electromagnetic characteristics of HTS LSM were studied. The results obtained show that (i) when the trapped magnetic field of BSCM increases to 2 T from 0.35 T, the F_x will increase by 3.3 times, which can't be realized by using conventional permanent magnets; (ii) when the length of BSCMs are located between 0.8τ and τ, the LSM will have better F_x performance; (iii) the F_x increases with increasing the thickness of BSCM when it is less than 20 mm; (iv) when the thickness of back-iron over 10 mm, the influence on F_x becomes saturated. Based on the above analysis, the HTS LSM can be optimized with HTS bulks and achieves better performance.

REFERENCES

[1] J. X. Jin, L. H. Zheng, Y. G. G, and J. G. Zhu, "Development of High Temperature Superconducting Machines," Journal of Japan Society of Applied Electromagnetics and Mechanics, vol. 15(s), pp. S88-S91, 2007.

[2] G. Stumberger, M. T. Aydemir, and A. L. Thomas, "Design of a linear bulk superconductor magnet synchronous motor for electromagnetic aircraft launch systems," IEEE Trans. Appl. Super., vol. 14, no. 1, pp. 54-62, 2004.

[3] J. X. Jin, and L. H. Zheng, "Performance analysis and optimization design of a HTS LSM," Journal of Science, Technology and Engineering, vol. 2, no. 1, pp. 19-22, 2008.

[4] A. Takahashi, H. Ueda, and A. Ishiyama, "Trial production and experiment of linear synchronous actuator with field-cooled HTS bulk secondary," IEEE Trans. Appl. Super., vol. 13, no. 2, pp. 2251-2254, 2003.

[5] K. Yoshida and H. Matsumoto, "Design and simulation of HTS bulk linear synchronous motor," Physica C, vol. 378-381, pp. 833-837, 2002.

[6] J. X. Jin, "High T$_c$ superconductor theoretical models and electromagnetic flux characteristics," Journal of Electronic Science and Technology of China, vol. 4, no. 3, pp. 202-208, September 2006.

[7] J. X. Jin and L. H. Zheng, "Verification of levitation force between a HTS and a permanent magnet," Physica C, vol. 460-462, pp. 1457-1458, 2007.

[8] Y. G. Guo, J.X. Jin, L.H. Zheng, J.G. Zhu, and H.Y. Lu, "A permanent magnet linear synchronous motor drive for HTS maglev Transportation Systems, " Journal of Electronic Science and Technology of China, vol .6, no. 2, pp. 125-129, June 2008.

[9] T. Suzuki, S. Araki, K. Koibuchi, K. Ogawa, K. Sawa, K. Takeuchi, et al, "A study on levitation force and its time relaxation behavior for a bulk superconductor-magnet system," Physica C, vol. 468, no. 15-20, pp. 1461-1464, 2008.

[10] F. C. Moon, K. C. Weng, and P. Z. Chang, "Dynamic magnetic forces in superconducting ceramics," J. Appl. Phys., vol. 66, pp. 5643-5645, 1989.